Vacancy Ordering and Bonding Competition in the Group 9 Tellurides M_xTe_2 (M = Rh, Ir; $0.75 \leq x \leq 2$): A Theoretical Study

Chi-Shen Lee and Gordon J. Miller*

Department of Chemistry, Iowa State University, Ames, Iowa 50010

Received June 4, 1999

The Rh−Te and Ir−Te binary systems for 50−78 atom % Te show remarkable differences in their phase and structural features at temperatures below 1100 °C. Extended Hückel calculations are employed to investigate the influence of various orbital interactions on these differences. In general, a strong interrelationship among valence electron count, orbital characteristics at and near the Fermi levels, and relative strengths of M−Te, Te−Te, and M−M orbital interactions control the occurrence and structures of various M_xTe_2 compounds ($0.75 \leq x \leq 2$). Stronger Ir−Te than Rh−Te orbital interactions lead to the different low-temperature structures of $IrTe_2$ (CdI_2-type) and $RhTe_2$ (pyrite-type), but then short and intermediate-range Te−Te interactions lead to the pyrite-type structure for the defect phases $M_{1-u}Te_2$. At temperatures above 600 °C, $RhTe_2$ (pyrite-type) is unstable relative to disproportionation to the "stuffed" CdI_2-type $Rh_{1+x}Te_2$ and the defect pyrite-type $Rh_{1-u}Te_2$. The Rh-rich phases, $Rh_{1+x}Te_2$, show ordered vacancies in alternating layers of octahedral holes and can be formulated as $(Rh_3)_x(Rh)_{1-2x}Te_2$ ($x \leq 1/2$) and $(Rh_3)_{1-x}(Rh)_{4x-2}Te_2$ ($x \geq 1/2$) to emphasize the occurrence of linear Rh_3 units in their structures. The pattern of vacancies in these structures follows the preference of Rh_{4n+3} oligomers over Rh_{4n+1} chains. Charge-iterative calculations of Rh atomic orbital energies in $Rh_{1+x}Te_2$ ($x = 0.0, 0.5, 1.0$) were carried out to analyze the electronic properties of Rh throughout the series. As x increases, Rh−Te orbital interactions become less attractive and the concentration of Rh−Rh repulsive interactions grows. Both effects control the maximum value of x (observed to be 0.84) for this series and influence the pattern of occupied octahedral holes in the close-packed tellurium matrix.

Introduction

Binary transition metal chalcogenides attract extensive investigation due to fundamental interest in the nature of their metal−metal, metal−chalcogenide, and chalcogenide−chalcogenide bonding, as well as their potential applications via electronic phase transitions and intercalation chemistry.[1] In particular, the dichalcogenides MX_2 (X = S, Se, Te) form either two-dimensional (2D) or three-dimensional (3D) structures,[2] depending on the identity of both M and X. According to thorough structural, physical, and theoretical investigations, the dimensionality of a particular dichalcogenide depends on the d electron count of the transition element and the relative energies of the metal d and chalcogen sp orbitals.[3] For the transition metal disulfides MS_2, Burdett and McLarnan have shown[4] that disulfide groups (S_2^{2-}) prevail if the enthalpy change for the process $M^{2+}(g) \rightarrow M^{4+}(g) + 2e^-$ exceeds ca. 80 eV. If this enthalpy change is less than 80 eV, isolated sulfide ions (S^{2-}) occur. Rouxel and co-workers generalized this concept for all chalcogenides by using a qualitative electronic energy band argument based on the relative electronegativities of the metal atoms and the chalcogen.[5] Their approach indicates a redox competition between the cation d and anion sp electronic band levels, which leads to various structural preferences and details, viz., interatomic distances. They have also established differences within various anionic partial structures depending upon the occurrence of intermediate range Te···Te interactions to produce "polymerized" Te networks.

Table 1. Atomic Orbital Energy Parameters for Extended Hückel Calculations

atom	orbital	H_{ii} (eV)	ζ_1	c_1	ζ_2	c_2
Te	5s	−20.80	2.51			
	5p	−14.80	2.16			
Rh	5s	−9.17	2.14			
	5p	−3.97	2.10			
	4d	−12.71	5.54	0.5561	2.40	0.6117
Ir	6s	−11.36	2.50			
	6p	−4.50	2.20			
	5d	−12.17	5.80	0.6698	2.56	0.5860
Rh ("$RhTe_2$")	5s	−9.65	2.14			
	5p	−4.26	2.10			
	4d	−13.56	5.54	0.5561	2.40	0.6117
Rh (Rh_3Te_4)	5s	−9.37	2.14			
	5p	−3.94	2.10			
	4d	−13.09	5.54	0.5561	2.40	0.6117
Rh ("RhTe")	5s	−8.68	2.14			
	5p	−3.23	2.10			
	4d	−11.92	5.54	0.5561	2.40	0.6117

Tellurium produces many different anionic groupings.[5] The transition metal ditellurides, with few exceptions, form either the CdI_2-type or the pyrite-type structure. Jobic et al. identify five different classes of ditellurides on the basis of tellurium−tellurium and metal−metal interactions:[2]

1. True 2D CdI_2-type phases: $ZrTe_2$ and $HfTe_2$ have nearly ideal c/a ratios of 1.68 and show no evidence for metal−metal bonding (i.e., no observed superstructures in the (001) planes exist). These are d^0 metal compounds.

(1) (a) Hulliger F. *Struct. Bonding* (Berlin) **1967**, *4*, 83. (b) Hulliger F. In *Structural Chemistry of Layer-Type Phases*; Levy, F., Ed.; Reidel: Dordrecht, The Netherlands, 1976.
(2) Jobic, S.; Brec, R.; Rouxel, J. *J. Alloys Compd.* **1992**, *178*, 253.
(3) Jobic, S.; Brec, R.; Rouxel, J. *J. Solid State Chem.* **1992**, *96*, 169.
(4) Burdett, J. K.; McLarnan, T. J. *Inorg. Chem.* **1982**, *21*, 1119.
(5) Rouxel, J. *Comments Inorg. Chem.* **1993**, *14*, 207.

10.1021/ic990652s CCC: $18.00
Published on Web 10/05/1999

Table 2. Results from EHT Calculations on $[MTe_6]$ and $[M(Te_2)_6]$ Fragments (eV)

	$[RhTe_6]$	$[IrTe_6]$	$[Rh(Te_2)_6]$	$[Ir(Te_2)_6]$
$E(t_{2g})$	−12.34 (3*x*)	−11.69 (3*x*)	−12.37 (2*x*) −12.18 (1*x*)	−11.88 (2*x*) −11.58 (1*x*)
$E(e_g)$	−9.31 (2*x*)	−8.10 (2*x*)	−9.43 (2*x*)	−8.61 (2*x*)
$E(Te_2\ \sigma_p^*)$			−9.19 to −7.78	−9.20 to −7.46
E(Te 5p)	−16.58 to −13.46	−16.85 to −13.46		
$E(Te_2\ \sigma_p, \pi, \pi^*)$			−17.10 to −12.59	−17.27 to −12.59

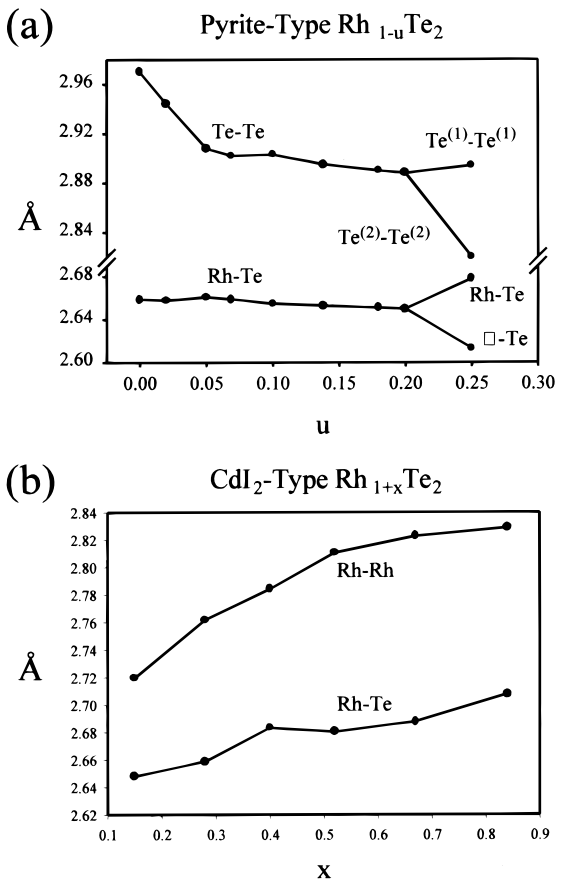

Figure 1. Top: Variations in the shortest Rh−Te and Te−Te distances in the defect pyrite-type $Rh_{1-u}Te_2$ phases as a function of *u*.[8] Bottom: Variations in the shortest Rh−Te and Rh−Rh distances in the stuffed CdI_2-type $Rh_{1+x}Te_2$ phases as a function of *x*[7].

2. 2D polymerized, distorted CdI_2-type phases: $MoTe_2$ and WTe_2 show through-layer and within-layer Te···Te "bonding" (ca. 3.66 and 3.50 Å, respectively, between these Te atoms). [In the CdI_2 structure for MTe_2, *within-layer* Te···Te "bonding" refers to a single plane of Te atoms, *through-layer* Te···Te "bonding" occurs between planes of Te atoms within each Te−M−Te slab, and *between-layer* Te···Te "bonding" occurs between planes of Te atoms between two Te−M−Te slabs.] Longer between-layer distances (greater than 4.00 Å) maintain the proposed 2D character of these phases. Significant metal−metal bonding also occurs as the 2D triangular net of metals distorts into ribbons.

3. 3D polymeric, 2D-derived CdI_2-type phases with metal−metal bonding: $NbTe_2$ and $TaTe_2$ show weak Te···Te polymerization between layers (ca. 3.60 Å) and significant metal−metal bonding within each layer.

4. 3D polymeric, 2D-derived CdI_2-type phases without metal−metal bonding: $IrTe_2$, $Rh_{1+x}Te_2$, $CoTe_{1.7}$, $PdTe_2$, and $PtTe_2$ show weak Te···Te "bonding" between layers as demonstrated by their low *c*/*a* ratios of ca. 1.27−1.38. No metal−metal bonding is apparent.

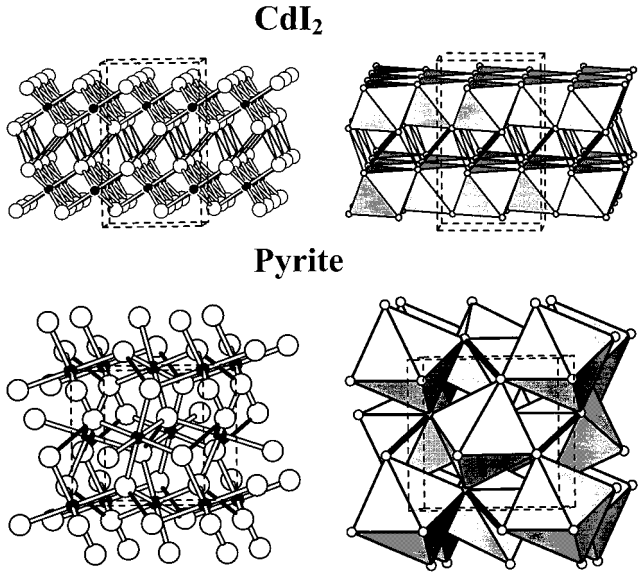

Figure 2. Ball-and-stick and polyhedral representations of the structures of CdI_2 (top) and pyrite (bottom). $IrTe_2$ adopts the CdI_2-type arrangement; $RhTe_2$ adopts the pyrite structure.

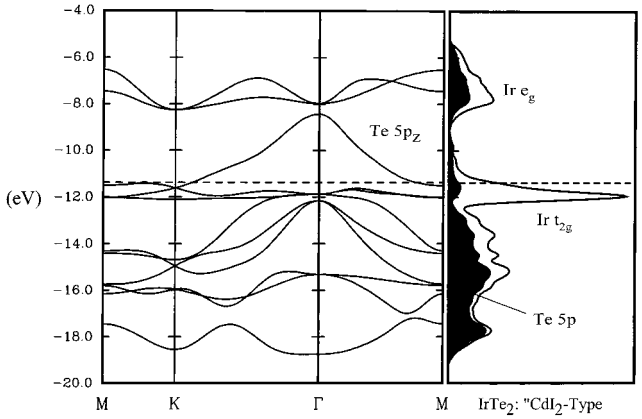

Figure 3. Energy band diagram and total DOS for $IrTe_2$ in the CdI_2 structure. The dashed line is the calculated Fermi level for $IrTe_2$. Various regions of the DOS are labeled, and the Te contribution to the total DOS is shaded in the DOS curve.

5. 3D pyrite-type (and marcasite-type) phases: $MnTe_2$, $FeTe_2$, $RuTe_2$, $OsTe_2$, $NiTe_2$, and $RhTe_2$ vary in the extent of weak Te···Te "bonding" with no metal−metal bonding apparent.

In all cases, each metal atom is coordinated by an octahedral environment of telluride-based ligands, which are either isolated telluride ions, ditelluride groups, or, as in type 4 compounds, a polymeric sheet of weakly interacting tellurium atoms. Furthermore, the formal oxidation states of the metal atoms range from +2 to +4. Metal−metal bonding occurs for the early transition elements with d^1−d^3 electronic configurations.

The observed trend in structures with d electron count and period of the transition metal is certainly striking.[2] For the fifth- and sixth-period metals, the group 9 elements (Rh and Ir)

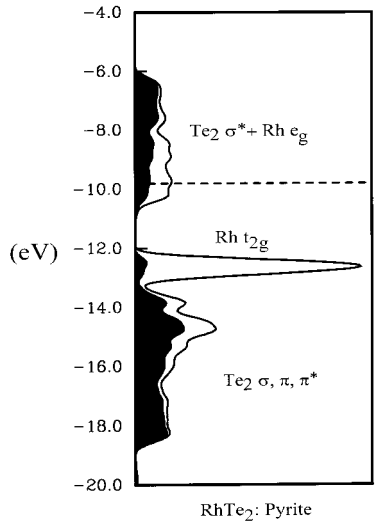

Figure 4. Total DOS for $RhTe_2$ in the pyrite structure. The dashed line is the calculated Fermi level for $RhTe_2$. Various regions of the DOS are labeled, and the Te contribution to the total DOS is shaded in the DOS curve.

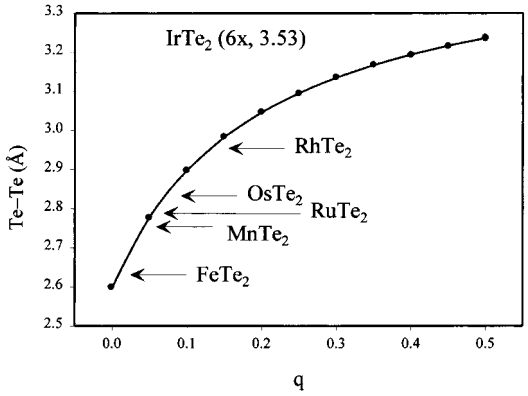

Figure 5. Variation in Te−Te distance with occupation of the σ_p* orbital in $(Te-Te)^{(2+q)-}$ dimers. At each point, the total valence electron energy is minimized for the given charge. Te−Te distances in several ditellurides are indicated on the graph.

represent a special transition point between the 3D pyrite-type and the 3D−polymerized 2D CdI_2-type structures. In fact, the equilibrium solid phases Rh_xTe_2 and Ir_xTe_2 in the neighborhood of MTe_2 exhibit interesting structural changes as self-intercalation processes and vacancy ordering occur at the metal sites in the telluride matrix.[7] This work specifically examines the structural preferences for these group 9 tellurides, M_xTe_2 ($0.75 \leq x \leq 2.00$), by analyzing the orbital interactions and valence electron concentrations involved for the various compounds. We will address the arrangement of vacancies and self-intercalated species from the viewpoint of metal−tellurium, metal−metal, and tellurium−tellurium orbital interactions and the types of local chemical environments that arise.

Phases in the Rh_xTe_2 and Ir_xTe_2 Systems

An examination of the binary phase diagrams for Rh−Te and Ir−Te shows expected similarities but still some remarkable differences between the equilibrium phases existing in these two systems. The information published for the Rh−Te system is more detailed,[8] and seemingly more complex, than that for the Ir−Te system.[9] Nevertheless, in the region 50−78 atom % tellurium, all structures are derived from either the CdI_2-type or the pyrite-type structures.

Comprehensive studies of the Rh_xTe_2 ($0.75 \leq x \leq 2.00$) system with respect to equilibrium phases and structural characterizations have been reported by Kjekshus et al.,[8] Krachler et al.,[10] and Abadie et al.[7] $RhTe_2$ adopts the pyrite structure, but cannot be obtained as a stoichiometric compound above 550 °C. At these higher temperatures, $RhTe_2$ is unstable relative to a combination of a defect pyrite-type ($Rh_{1-u}Te_2$) and a self-intercalated CdI_2-type ($Rh_{1+x}Te_2$). Above ca. 1100 °C, $Rh_{1+x}Te_2$ and "Te"(l) (an unknown liquid phase) are the equilibrium phases. In fact, a 2D (or, rather, polymerized 2D) structure of stoichiometric "$RhTe_2$" is never reported. The defect pyrite-type phases, $Rh_{1-u}Te_2$, show no ordering of vacancies on the metal sites above 400 °C for $u < 0.20$. $Rh_{0.75}Te_2$ ($u = 0.25$), or Rh_3Te_8, exhibits rhombohedral symmetry with an ordering of vacancies in the pyrite-type framework and decomposes peritectically at ca. 630 °C to $Rh_{1-u}Te_2$ and Te.[8] Structural characterization of these phases reveals trends in Rh−Te and

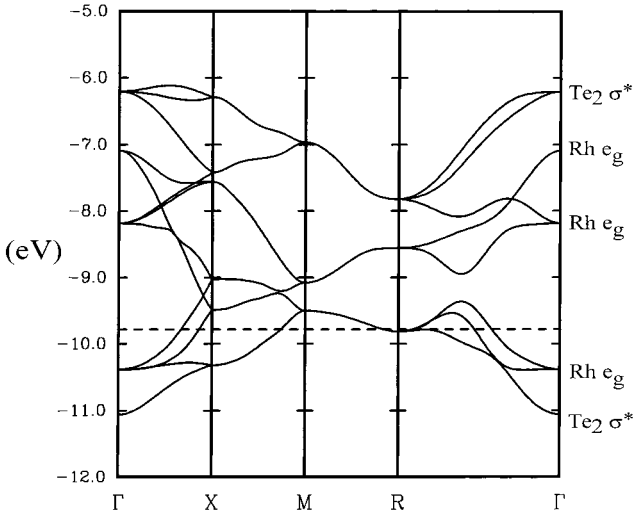

Figure 6. Energy band dispersion curves for the e_g/σ_p* bands in $RhTe_2$. The dashed line is the calculated Fermi level for $RhTe_2$. Crystal orbitals at the zone center (Γ) are labeled.

Table 3. Results of EHT Calculations on CdI_2- and Pyrite-Type Structures for $RhTe_2$ and $IrTe_2$ Using Various Cutoff Distances for the Inclusion of Interatomic Orbital Overlaps[a]

	$RhTe_2$		$IrTe_2$	
	pyrite-type	CdI_2-Type	pyrite-type	CdI_2-type
M−Te (Å)	2.66 (6*x*)	2.57 (6*x*)	2.71 (6*x*)	2.64 (6*x*)
	4.10 (2*x*)	4.54 (6*x*)	4.01 (2*x*)	4.65 (6*x*)
	4.26 (6*x*)	4.61 (4*x*)	4.52 (6*x*)	4.73 (4*x*)
Te−Te (Å)	2.97 (1*x*)	3.45 (6*x*)	3.44 (1*x*)	3.53 (6*x*)
	3.56 (6*x*)	3.83 (6*x*)	3.56 (6*x*)	3.93 (6*x*)
	3.95 (6*x*)		4.08 (6*x*)	
M−M (Å)	4.56 (12*x*)	3.83 (6*x*)	4.67 (12*x*)	3.93 (6*x*)
	Total Valence Electron Energies (eV)			
$\rho = 3.55$ Å	0.00	0.52	0.00	1.14
$\rho = 3.60$ Å	1.83	0.52	3.09	1.14
$\rho = 3.90$ Å	1.83	2.47	3.09	1.14
$\rho = 4.05$ Å	3.49	2.47	3.62	3.23

[a] Short and intermediate range distances are listed.

(6) Böttcher, P. *Angew. Chem.* **1988**, *100*, 781; *Angew. Chem., Int. Ed. Engl.* **1988**, *27*, 759.
(7) Abadie, V.; Jobic, S.; Krachler, R.; Ipser, H.; Orion, I.; Brec, R. *J. Alloys Compd.* **1998**, *268*, 50.
(8) Kjekshus, A.; Rakke, T.; Andersen, A. F. *Acta Chem. Scand.* **1978**, *A32*, 209.
(9) Hocking, E. F.; White, J. G. *J. Phys. Chem.* **1960**, *64*, 1042.
(10) Krachler, R.; Ipser, H. *Z. Metallkd.* **1996**, *87*, 262.

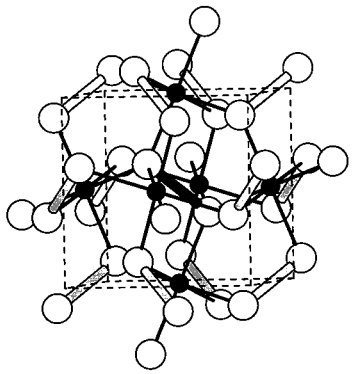

Figure 7. Crystal structure of Rh_3Te_8. Shaded circles are Rh atoms; open circles are Te atoms. The short Te−Te dimers are indicated by the solid black bar; the longer Te−Te dimers are shown by the shaded bars. Rh−Te contacts are solid lines. The unit cell is also indicated by the dashed lines.

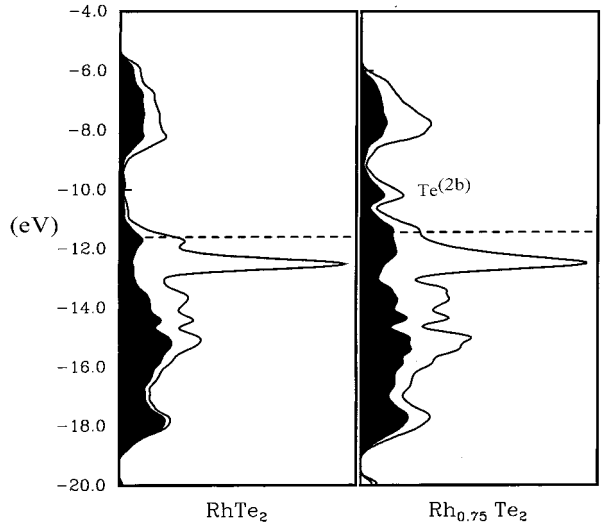

Figure 8. Total DOS curves for (left) $RhTe_2$ and (right) $Rh_{0.75}Te_2$ in the CdI_2-type structures (both are hypothetical models). The projections of Te atomic orbitals to the total DOS are shown. The dashed lines correspond to the calculated Fermi levels. The peak in the DOS of $Rh_{0.75}Te_2$ below −10.0 eV, which is absent in the DOS of $RhTe_2$, is a strong admixture of orbitals from the two-coordinate Te atoms ($Te^{(2b)}$) and Rh atoms.

Te−Te distances shown in Figure 1. Note the sharp drop in the Te−Te distance as u increases from 0 to 0.1 in $Rh_{1-u}Te_2$, while there is little change in the Rh−Te distance. Furthermore, rhombohedral Rh_3Te_8 shows two crystallographically inequivalent Te−Te dimers in a 3:1 ratio and, likewise, two distinct Te−Te distances. The vacancy sites in the metal substructure are surrounded by six shorter dimers (Te−Te: 2.82 Å), and each Rh site is coordinated by four shorter and two longer dimers (Te−Te: 2.89 Å).

The Rh-rich phases, $Rh_{1+x}Te_2$, have been prepared and structurally characterized for various compositions, $0.15 \leq x \leq 0.84$.[7] Rh can be gradually added to the interlayer sites of a CdI_2-type "$RhTe_2$" to form the observed series of compounds intermediate between the CdI_2-type and the NiAs-type. Three distinct types of phases were identified by this study. $Rh_{1.15}Te_2$ adopts a hexagonal CdI_2-type structure with the layers of octahedral holes in the Te close-packed matrix occupied alternately 100% and 15% by Rh atoms. $Rh_{1.52}Te_2$ forms in the monoclinic Cr_3S_4-type structure with alternating metal occupancies of 100% and 52% in the sheets of octahedral holes. Finally, $Rh_{1.84}Te_2$ is a defect, hexagonal NiAs-type, with 100% and 84%

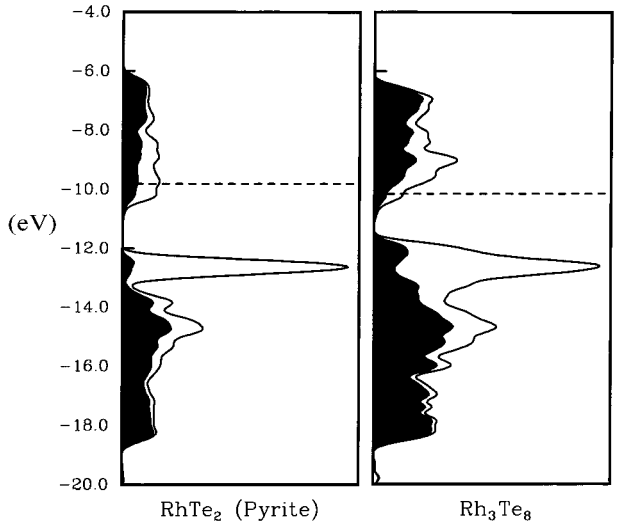

Figure 9. Total DOS curves for (left) $RhTe_2$ and (right) $Rh_{0.75}Te_2$ in the pyrite-type structures. The projections of Te atomic orbitals to the total DOS are shown. The dashed lines correspond to the calculated Fermi levels. The strong peaks in both DOS curves near −12.5 eV are Rh t_{2g} orbitals. The appearance of a shoulder at −12.0 eV in the DOS of Rh_3Te_8 below −10.0 eV, which is absent in the DOS of $RhTe_2$, is assigned to orbitals from Te atoms surrounding each metal site vacancy in the pyrite network.

Table 4. Results from Extended Hückel Calculations on $M_{1-u}Te_2$ for Defect CdI_2-Type and Pyrite-Type Structures

u(Pyrite)	E_F (eV)	q(Rh)	q(Te)	p(Rh−Te)	p(Te−Te)
0.0	−9.80	9.36	5.82	0.250	0.215
0.125	−9.91	9.19	5.78 ($^5/_8$)	0.257	0.225
			6.14 ($^3/_8$)		
0.25	−10.20	9.04	5.72 ($^1/_4$)	0.270	0.227
			6.09 ($^3/_4$)		0.239 (3x)
					0.191 (1x)
u(CdI_2)	E_F (eV)	q(Rh)	q(Te)	p(Rh−Te)	p(Te−Te)
0	−11.62	8.98	6.01	0.289	0.034
0.25	−11.44	8.88	5.79 ($^1/_4$)	0.328	0.025
			6.13 ($^3/_4$)		

alternating octahedral site occupancies. In fact, for the observed range of compositions, a monoclinic unit cell (a nearly pseudoorthorhombic setting of the hexagonal CdI_2 aristo-type) can describe the structures of all $Rh_{1+x}Te_2$ phases. The two crystallographic sites for the intercalated Rh atoms are occupied in an ordered fashion throughout the range. For $x \leq 0.5$, one metal site remains empty, while the other fills to the extent of $2x$. For $x \geq 0.5$, the metal site filled for $x = 0.5$ remains filled, while the other fills to the extent of $2x$. The significance of this pattern is that linear Rh−Rh−Rh groups, which align parallel to the pseudohexagonal axis, are important components of $Rh_{1+x}Te_2$. As x increases, average Rh−Te distances monotonically increase from 2.65 to 2.71 Å and Rh−Rh distances (in the Rh_3 units) increase from 2.72 to 2.83 Å (see also Figure 1).

The corresponding Ir−Te system in the same composition regime shows only two confirmed compounds, $IrTe_2$ and Ir_3Te_8, and a proposed IrTe phase.[9] $IrTe_2$, unlike $RhTe_2$, adopts the CdI_2-type structure. With its small c/a ratio of 1.37 ($a = 3.928$ Å, $c = 5.381$ Å), Jobic et al. contend that there is some weak Te···Te "bonding" between each Te−Ir−Te layer.[2,11] Ir_3Te_8, on the other hand, is isostructural with Rh_3Te_8.[12] In $IrTe_2$ and

(11) Jobic, S.; Evain, M.; Brec, R.; Rouxel, J.; Jouanneaux, A.; Fitch, A. N. *Z. Anorg. Allg. Chem.* **1991**, *598*, 199.
(12) Brostingen, G.; Kjekshus, A. *Acta Chem. Scand.* **1970**, *24*, 2993.

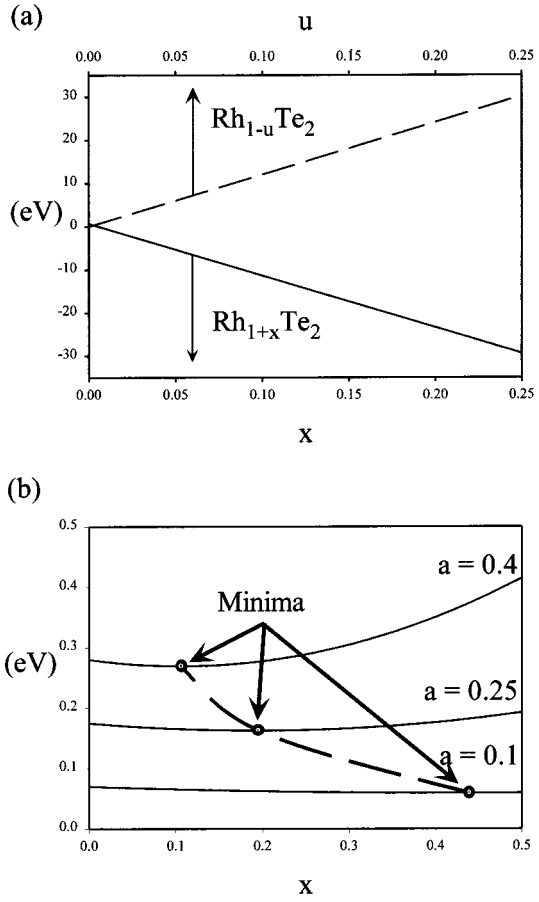

Figure 10. (a) Variations in total valence electron energies with stoichiometric variables u and x in $Rh_{1-u}Te_2$ (defect pyrite-type) and $Rh_{1+x}Te_2$ (stuffed CdI_2-type). At $RhTe_2$, the pyrite structure is preferred by ca. 0.7 eV. (b) $\Delta E(x)$ curves for the disproportionation of $RhTe_2$(c) into $Rh_{1-u}Te_2$ (defect pyrite-type) and $Rh_{1+x}Te_2$ (stuffed CdI_2-type) for various fractions of $Rh_{1+x}Te_2$ (stuffed CdI_2-type), indicated by a. The minima for each curve are indicated, and these points are connected by the dotted line.

Ir_3Te_8, the Ir−Te distances are 2.65 Å while the Te−Te distances are ca. 2.88 Å in Ir_3Te_8. No details concerning possible intermediate phases $Ir_{1+x}Te_2$ have yet been reported.

Methods

The main object of this paper is to elucidate reasons for the observed phases and structures in the group 9 tellurides M_xTe_2 using orbital symmetry arguments. The electronic structures of the actual as well as many hypothetical structures were calculated using the LCAO (tight-binding) approximation with the extended Hückel theory.[13] Atomic orbital parameters of a minimal basis set for Rh, Ir, and Te are listed in Table 1. Integrations for total valence electron energies, Mulliken populations, and overlap populations were performed using special-point sets of 50−200 **k**-points in the corresponding irreducible wedges of the first Brillouin zones for these structures.[14] For the series $Rh_{1+x}Te_2$ ($0 \le x \le 1$), the atomic orbital energies for Rh were evaluated in a self-consistent manner, and these values are also listed in Table 1. Further specifics of each calculation are described in the subsequent text.

(13) (a) Hoffmann, R.; Lipscomb, W. N. *J. Chem. Phys.* **1962**, *36*, 3179, 3189. (b) Hoffmann, R. *J. Chem. Phys.* **1963**, *39*, 1397. (c) Ammeter, J. H.; Bürgi, H.-B.; Thibeault, J. C.; Hoffmann, R. *J. Am. Chem. Soc.* **1978**, *100*, 3686. (d) Whangbo, M.-H.; Hoffmann, R.; Woodward, R. B. *Proc. R. Soc. London, Ser. A* **1979**, *366*, 23.

(14) (a) Chadi, D. J.; Cohen, M. L. *Phys. Rev. B: Condens. Matter* **1975**, *12*, 3060. (b) Ramírez, R.; Böhm, M. C. *Int. J. Quantum Chem.* **1986**, *30*, 391. (c) Ramírez, R.; Böhm, M. C. *Int. J. Quantum Chem.* **1988**, *34*, 571.

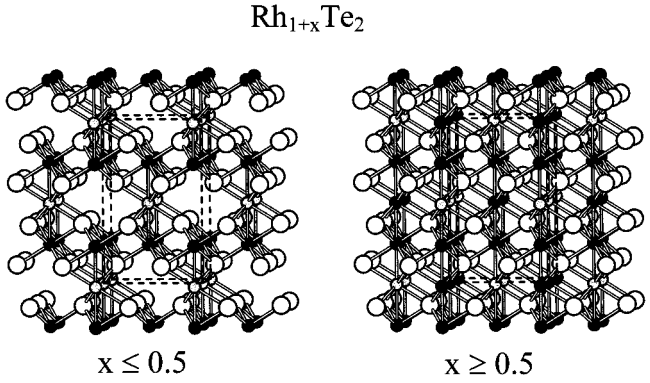

Figure 11. Crystal structures of $Rh_{1+x}Te_2$. Open circles are Te atoms. Filled, black circles are completely occupied Rh sites. Shaded gray circles are partially occupied Rh sites. The shortest Rh−Te and Rh−Rh distances are indicated.

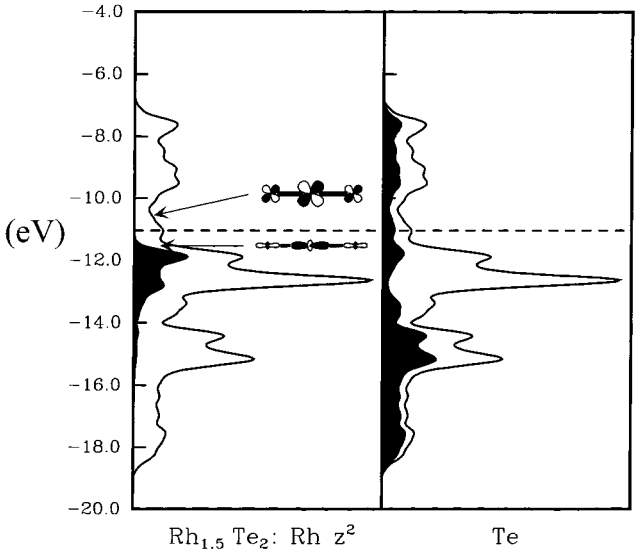

Figure 12. Total DOS curve for $Rh_{1.5}Te_2$ with projections from Rh z^2 orbitals and Te atomic orbitals highlighted. The dashed line indicates the calculated Fermi level. The top of the z^2 orbitals is Rh−Rh σ^* with the higher orbital coefficient on the central Rh atom ($Rh^{(c)}$). Orbitals just above the Fermi level show Rh−Rh π^* character as indicated by its orbital representation.

Metal Ditellurides: CdI_2-Type or Pyrite-Type?

One unusual feature of the group 9 ditellurides is the different low-temperature structures for $RhTe_2$ and $IrTe_2$. While $IrTe_2$ adopts the CdI_2-type structure, $RhTe_2$ forms in the pyrite-type and needs some additional Rh atoms to achieve the layered morphology, e.g., $Rh_{1.15}Te_2$ (see Figure 2 for "ball-and-stick" and polyhedral representations of each structure). Although both Jobic et al.[2] as well as Burdett et al.[4] have addressed factors leading to one structure type or the other, neither has focused on the group 9 problem in particular. According to the structural formulas for each type, $^2_\infty[MTe_{6/3}]$ and $^3_\infty[M(Te_2)_{6/6}]$, we must consider not only the M-to-Te charge transfer but also the relative strengths of the octahedral ligand fields created by six telluride, $[-Te_6]$, and six ditelluride groups, $[-(Te_2)_6]$. Table 2 summarizes molecular orbital energies for calculations on four "isolated" ML_6 octahedral fragments: (a) $[RhTe_6]$, (b) $[Rh(Te_2)_6]$, (c) $[IrTe_6]$, and (d) $[Ir(Te_2)_6]$. In the ditelluride fragments b and d, the M−Te−Te angle is set at 98.5°, which is the observed Rh−Te−Te angle in $RhTe_2$. With this structural feature, the metal e_g orbitals will overlap strongly with one of the π^* orbitals from each Te_2 unit in a σ fashion (**1**) and very

weakly with the six Te_2 σ_p* orbitals (**2**). The M−Te σ-bonding

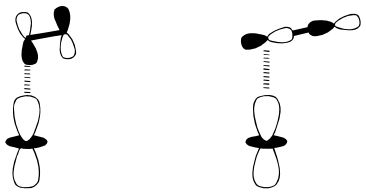

1 **2**

e_g orbitals lie well within the occupied Te 5p orbitals, but the M−Te σ-antibonding e_g orbitals rise to an energy comparable to that calculated for the Te_2 σ_p* orbital, as seen in Table 2.

The results from Table 2 may be summarized as follows:

(1) Δ_{oct} values for $[IrTe_6]$ and $[Ir(Te_2)_6]$ (3.59 and 3.28 eV, respectively) exceed those for $[RhTe_6]$ and $[Rh(Te_2)_6]$ (3.03 and 2.94 eV, respectively). Ir−Te orbital interactions are stronger than Rh−Te interactions due to the relativistic contraction of the Ir valence atomic orbitals relative to Rh. The relativistic effect produces similar sizes for Ir and Rh atoms[15] but larger overlap integrals (S_{ij}) for Ir−Te interactions than for Rh−Te interactions. On the other hand, the M d−Te 5p atomic orbital energy difference, $\Delta E^{(0)}$, is larger for Ir than for Rh. Since orbital interactions are measured as $S^2/|\Delta E^{(0)}|$, the overlap term controls the relative energies of the fragment molecular orbitals.

(2) Weak Te···Te second nearest neighbor interactions create a "band" of six Te_2 σ_p* orbitals. These overlaps, however, are sufficiently large that the bottom of the Te_2 σ_p* "band" drops below the energy of the Ir e_g orbitals within this band but not that of the Rh e_g orbitals.

As these molecular fragments condense into their respective extended solids, all orbitals broaden into quasicontinuous energy bands. In the CdI_2 structure, inter- and intralayer Te···Te interactions push the top of the Te 5p band above the M t_{2g} orbitals (see Figure 3, which illustrates the total density of states (DOS) and energy bands for $IrTe_2$). There are a sufficient number of holes in the Te 5p band to create a weakly attractive Te···Te interaction between MTe_2 layers, as indicated by their slightly positive overlap population (+0.034 in "$RhTe_2$"; +0.007 in $IrTe_2$). This weak "bonding" is the basis for assigning these compounds to the 3D polymeric, 2D derived structures.[2] As the band structure illustrates, these holes are associated with states surrounding the zone center in the Brillouin zone. Furthermore, the M t_{2g} orbitals are filled. Since the M e_g band remains well above the Fermi level, the formulation $M^{3+}(Te^{1.5-})_2$ is appropriate for these hexagonal group 9 ditellurides and the Te substructure is a weakly bonded 3D polymerized net.

In the pyrite structure, the Te_2 σ_p* orbital splits away from the other Te 5p bands and into the energy range of M e_g orbitals (see Figure 4, which shows the total DOS for $RhTe_2$). This collection of three orbitals per formula unit constitutes the conduction band for the group 9 pyrite-type ditellurides and obtains one electron per formula unit. Depending on the relative energies of M e_g and Te_2 σ_p* orbitals, the formulation can range, in principle, from $M^{2+}(Te_2)^{2-}$ (i.e., d^7 M^{2+}, σ_p* empty) to $M^{3+}(Te_2)^{3-}$ (i.e., d^6 M^{3+}, σ_p* half-filled). The DOS shows, however, that the correct formulation for these compounds is some intermediate description.

Figure 5 illustrates the Te−Te distance that minimizes the total valence electron energy of the dimer $(Te_2)^{(2+q)-}$ for a given value of q. Since the ground-state electronic configuration of

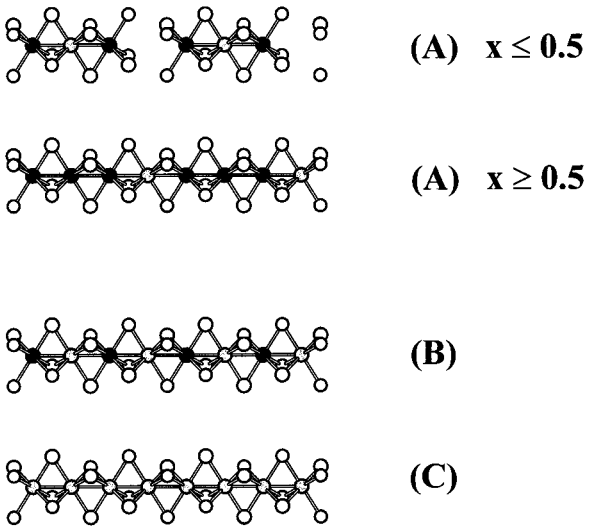

Figure 13. Three possible patterns for filling octahedral holes in $Rh_{1+x}Te_2$. Open circles are Te atoms; black circles are completely occupied metal sites; gray circles are partially occupied metal sites. Only a single chain of metal atom sites is illustrated (for clarity).

$(Te_2)^{(2+q)-}$ is $(\sigma_s)^2(\sigma_s^*)^2(\sigma_p)^2(\pi)^4(\pi^*)^4(\sigma_p^*)^q$, q represents the population of the antibonding σ_p* orbital. Figure 5 also indicates Te−Te distances for various transition metal ditellurides. A Mulliken population analysis on pyrite-type $RhTe_2$ and "$IrTe_2$" indicates that the occupied part of the e_g/σ_p* band is 61% Rh, 39% Te in $RhTe_2$ and 55% Ir, 45% Te in "$IrTe_2$". From this result and Figure 5, we can conclude that Te is more reduced with Ir in $IrTe_2$ than with Rh in $RhTe_2$ and that $RhTe_2$ has a stronger tendency to form the pyrite-type structure than does $IrTe_2$.

Intermediate-range Te···Te interactions are also influential in the structural chemistry of tellurides. For the group 9 ditellurides, these interactions are repulsive and sensitive to distance because the orbitals involved have Te···Te antibonding character. Table 3 lists short and intermediate-range distances in $RhTe_2$ and a pyrite-type "$IrTe_2$". Also listed are the total valence electron energies for different cutoff distances for the calculation of orbital overlaps (when interatomic distances are greater than this cutoff value, overlap matrix elements, S_{ij}, are set to zero). When the cutoff is 3.90 Å (close to the van der Waals diameter of Te), the correct "prediction" occurs: $RhTe_2$ prefers the pyrite-type; $IrTe_2$ prefers the CdI_2-type. When just the shortest M−Te and Te−Te interactions are used, the pyrite-type structure is preferred. As more orbital overlaps are included (these are mostly intermediate-range Te−Te interactions), the CdI_2-type becomes favored for both cases, which points to the sensitivity of the Te 5p−5p orbital interactions to distance. The intermediate and longer range Te−Te interactions, which are repulsive as indicated by the calculated shifts in total energy values listed in Table 3, are overestimated by the single-ζ Slater-type functions assigned to Te. Nevertheless, the calculations demonstrate that these interactions play a critical role in determining structural preference.

The choice of pyrite or CdI_2 for the structures of group 9 ditellurides (21 valence electrons per formula unit) therefore depends on the relative occupation of the M e_g and the Te_2 σ_p* orbitals, i.e., $(e_g)^x(\sigma_p^*)^{1-x}$, in a pyrite-type structure. The larger x is, the greater is the tendency to adopt the pyrite arrangement. Due to M−Te, Te−Te, and Te···Te interactions, the value of x depends not only on the energies of the M e_g and Te_2 σ_p* orbitals but also on their respective bandwidths. The e_g bandwidth arises from through-bond $M-Te_2-M$ interactions, and the σ_p* band-

(15) (a) Pitzer, K. S. *Acc. Chem. Res.* **1979**, *12*, 271. (b) Pyykkö, P. *Chem. Rev.* **1988**, *88*, 563.

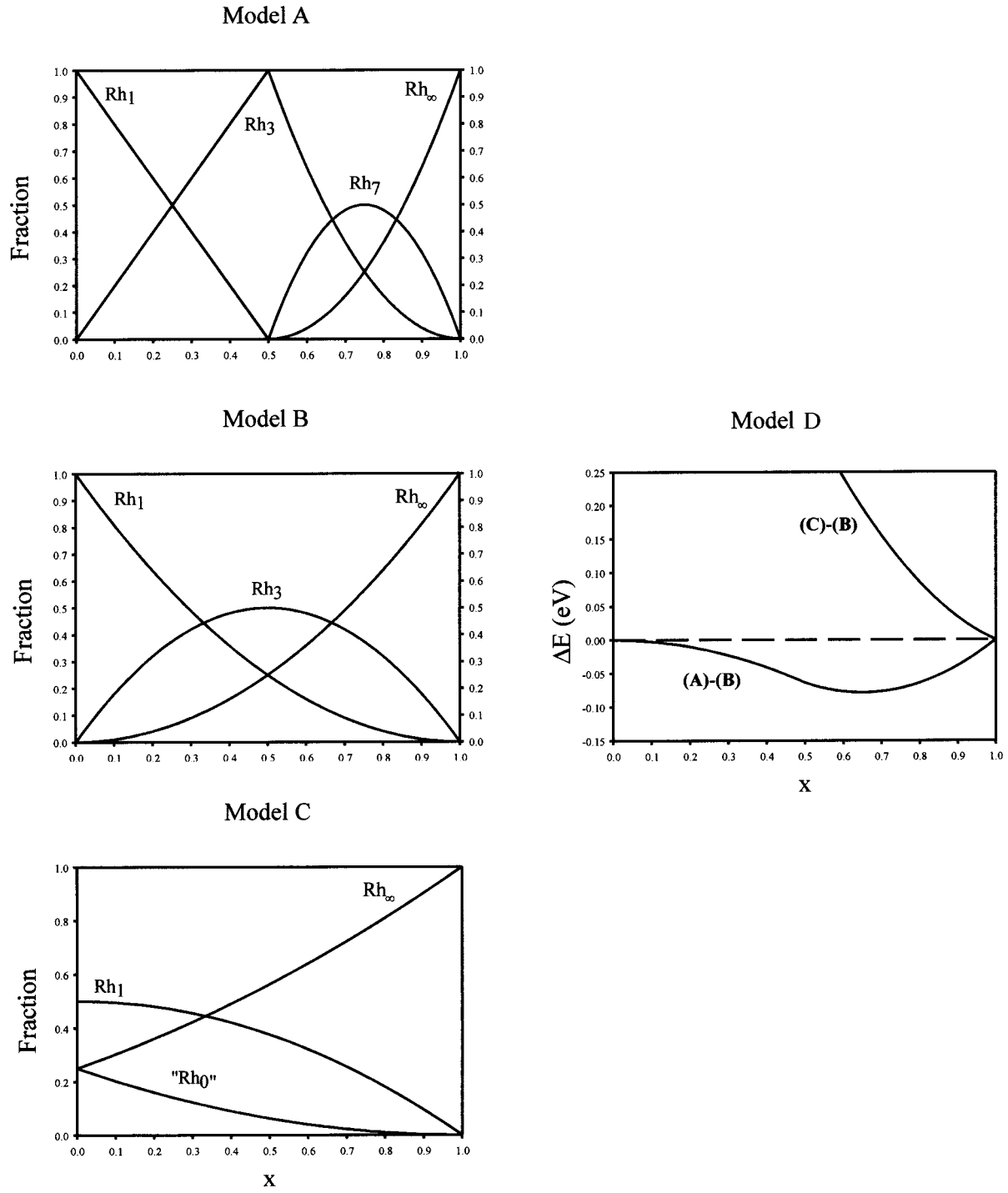

Figure 14. Left: Variations in fractions of Rh oligomers vs x for $Rh_{1+x}Te_2$ using the three models illustrated in Figure 13. Right: Relative total valence electron energies between these models vs x.

width, from through-space Te···Te and through-bond Te_2-M-Te_2 interactions. The band structure calculated for pyrite-type $RhTe_2$ in Figure 6 shows how these two sets of orbitals are affected by these interactions. In the band structure, there are eight Rh e_g-related bands and four Te_2 σ_p*-related bands because there are four formula units per unit cell. The bandwidths are essentially set by the respective band (orbital) energies at the zone center (symmetry is isomorphous with the group T_h). The Rh e_g bands all show gerade character, while the Te_2 σ_p* bands have ungerade character. Therefore, symmetry allows these bands to cross. The very bottom of this e_g/σ_p* band has completely σ_p* character, since the translational symmetry imposes a combination of Te_2 σ_p* orbitals that cannot overlap with Rh 5d orbitals and shows slight Te···Te attractive orbital overlaps. Away from the zone center, Rh 5d−Te 5p overlaps rapidly push this band to higher energy, where it eventually crosses the lowest Rh e_g band. In a hypothetical pyrite-type "$IrTe_2$", this band crossing occurs at a higher energy value, such that the Te_2 σ_p* orbitals would receive more electrons than in $RhTe_2$. Thus, we find $IrTe_2$ in the CdI_2 structure type.

Vacancies in the Metal Sites of MTe_2

$Rh_{1-u}Te_2$ has been characterized as a defect-pyrite-type structure for $u \leq 0.2$ with random vacancies on the Rh sites. At $u = 0.25$, $Rh_{0.75}Te_2$ (i.e., Rh_3Te_8) forms with a slight rhombohedral distortion and an ordered vacancy distribution

Table 5. Results from Extended Hückel Calculations on $M_{1+x}Te_2$ for Various Values of x[a]

x	E_F (eV)	q(Rh$^{(o)}$)	q(Rh$^{(t)}$)	q(Rh$^{(c)}$)	q(Te$^{(7)}$)	q(Te$^{(8)}$)	q(Te$^{(9)}$)	q(Te$^{(10)}$)	p(Rh−Te)	p(Rh−Rh)
0.000	−11.6	8.86			6.07				0.30	
0.083	−11.8	8.65	8.71	8.22	6.27	6.01			0.31	−0.01
0.167	−11.7	8.71	8.81	8.44	6.31	6.05			0.31	−0.02
0.250	−11.6	8.81	8.88	8.56	6.30	6.10	6.04		0.30	−0.03
0.333	−11.4	8.79	8.90	8.61	6.38	6.13	5.93		0.28	−0.02
0.500	−11.2		8.96	8.90		6.12	5.97		0.29	−0.02
0.667	−11.1	9.11	9.01	9.12		6.15	5.97	5.78	0.27	−0.02
0.750	−11.0	9.11	9.04	9.14			5.96	5.78	0.26	−0.02
0.833	−10.9	9.13	9.06	9.23			5.98	5.79	0.26	−0.01
1.000	−10.6	9.32						5.68	0.24	−0.03

[a] q = Mulliken population; p(A−B) = overlap population between atoms A and B. See Text for descriptions of Rh$^{(o)}$, Rh$^{(c)}$, and Rh$^{(t)}$. Te$^{(7)}$, Te$^{(8)}$, Te$^{(9)}$, and Te$^{(10)}$ correspond to the Te environments illustrated in **7**−**10**.

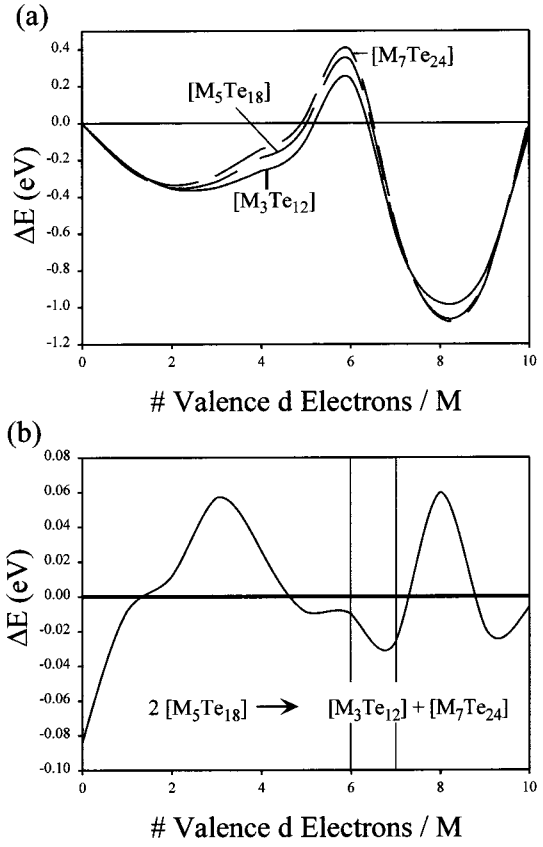

Figure 15. (a) Relative total valence electron energies vs d electron concentration among the oligomers $[Rh_3Te_{12}]$, $[Rh_5Te_{18}]$, and $[Rh_7Te_{24}]$ with respect to the isolated $RhTe_6$ octahedral fragment. (b) Relative total valence electron energy vs d electron concentration between $[Rh_3Te_{12}] + [Rh_7Te_{24}]$ and $2[Rh_5Te_{18}]$.

(see Figure 7).[8] Although the rhombohedral lattice constants show very slight changes from the trend in cubic phases, significant differences occur for Te−Te distances. In the unit cell, three Te_2 dimers shorten from ca. 2.89 to 2.82 Å and one Te_2 dimer slightly lengthens (see Figure 1). Ir_3Te_8 is isotypic with Rh_3Te_8, but there are no reports to our knowledge of $Ir_{1-u}Te_2$.[12] There are two important outcomes of these observations: (1) vacancies on the metal sites destabilize the CdI_2-type relative to the pyrite-type structure and (2) the vacancies affect the bonding in Te−Te dimers for group 9 systems.

To address the first point, we begin with the CdI_2 structure of MTe_2. Creating metal vacancies in this structure for the group 9 ditellurides removes electrons from the Te 5p band at a rate of 3 times the fraction of vacancies formed. In $M_{1-u}Te_2$, the number of orbitals in the valence band is $11 - 3u$ (this number arises from 4 AO's per Te atom plus $3(1 - u)$ t_{2g} orbitals per M atom; $2(1 - u)$ e_g orbitals remain unoccupied). The maximum number of valence electrons for the valence band is $2(11 - 3u) = 22 - 6u$, while the actual number is $21 - 9u$ ($=9(1 - u) + 2 \times 6$). The difference between these two values is $1 + 3u$, which identifies the number of holes in the valence band for $M_{1-u}Te_2$. Structurally, $6u$ Te atoms per formula unit become two-coordinate to the metal as vacancies arise, while the $2 - 6u$ remaining Te atoms remain three-coordinate. This difference in coordination environments leads to two distinct Mulliken populations for the Te sites. Enhanced Te···Te lone pair−lone pair repulsions keep the top of the Te 5p band high in energy, so there is a slight increase in the Fermi level. This enhancement in Te···Te repulsions arises because Te 5s orbitals are allowed to mix with 5p orbitals at the two-coordinate sites due to the reduction in site symmetry. Table 4 summarizes computational results for $Rh_{1-u}Te_2$ and $Ir_{1-u}Te_2$, $u = 0$ and 0.25, and Figure 8 illustrates the total DOS for $Rh_{1-u}Te_2$, $u = 0$ and 0.25. The small peak in the DOS of $Rh_{0.75}Te_2$ near the Fermi level corresponds to primarily the lone pair orbitals on the two-coordinate Te atoms (this peak is absent in the DOS of $RhTe_2$). The low Mulliken population for the three-coordinate Te sites in this (hypothetical) defect-CdI_2 model creates the driving force for forming Te−Te bonds, and this structure is unstable with respect to the defect pyrite-type.

Now, as metal atoms are removed from the pyrite network, the occupied fraction of the e_g/σ_p^* band drops. For $M_{1-u}Te_2$, this band has $3 - 2u$ orbitals per formula unit ($2 - 2u$ M e_g plus 1 Te_2 σ_p^* orbital) and $1 - 3u$ electrons per formula unit occupying them. Therefore, the occupied fraction varies with u as $(1 - 3u)/(6 - 4u)$: this band becomes empty at $u = {}^1/_3$, i.e., $M_{2/3}Te_2$. Observations show, however, that u reaches a maximum value at 0.25, which represents, on average, one metal site per cubic unit cell. Presumably, the lattice strain created by a vacancy concentration exceeding 25% is not overcome by an electronic driving force to optimize M−Te and Te−Te bonding.

$M_{0.75}Te_2$ ($u = 0.25$) compounds show an ordering of vacancies on the metal network, which gives rise to a rhombohedral structure M_3Te_8. All M atoms are crystallographically equivalent, while there are two distinct Te_2 dimers in a 3:1 ratio (see Figure 7 for an illustration of this structure; the two different Te_2 dimers are noted). The ideal formulation is $(M^{3+})_3(Te_2)^{3-}(Te_2)^{2-}{}_3$, which corresponds to empty M e_g orbitals and one electron in a single Te_2 σ_p^* orbital. As the DOS in Figure 9 shows, there is still some electron density in the M e_g orbitals. Furthermore, the bottom of the e_g/σ_p^* band does not change significantly, since it originates largely from the σ_p^* orbitals on the Te_2 groups. The most visible difference between the densities of states for $RhTe_2$ and Rh_3Te_8 occurs just above the Rh t_{2g} orbitals, where there is a significant

increase in the contribution from one of the Te_2 dimers. In Rh_3Te_8, one Te_2 dimer is coordinated to six Rh atoms (**3**); the other three are coordinated to four Rh atoms (**4**), which leaves

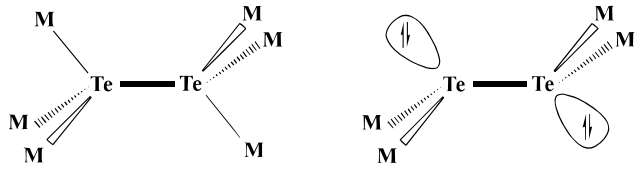

3 **4**

a lone pair of electrons on each Te atom. The peak in the DOS above the Rh t_{2g} orbitals corresponds to these lone pairs. In terms of a delocalized picture, this peak arises via orbital mixing. Since the Te_2 environment in **4** retains its inversion center, orbital mixing can only take place between gerade or between ungerade orbitals. We assign this small peak to one combination of the mixing between Te_2 σ_p and π^* orbitals (both gerade) (**5a**), which pushes the energy of these π^* orbitals above the

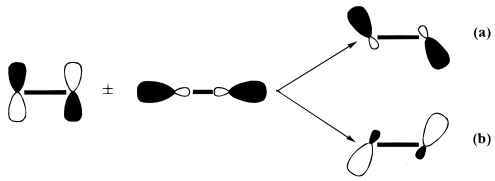

5

Rh t_{2g} orbitals. The other combination (**5b**) is near the bottom of the occupied Te_2 orbitals. As shown in **5a**, this orbital mixing also reduces the strength of the π^* overlap, which provides a driving force for shortening the distances in these Te−Te dimers. For a model of Rh_3Te_8 based on the cubic pyrite structure and all equal Te−Te distances, the calculated overlap populations indicate two distinctly inequivalent Te−Te bonds (see Table 4), which agrees with experiment and the qualitative analysis above.

The ordered arrangement of vacancies in Rh_3Te_8 creates just two types of Te−Te dimers (**3** and **4**). Randomizing the vacancy sites would also create five-coordinate Te_2 groups (**6**). The

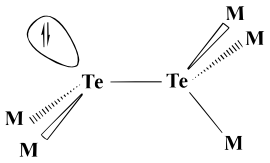

6

energy for the process **3** + **4** → 2 **6** is estimated to be +2.6 eV, which suggests that minimizing the number of five-coordinate Te_2 groups minimizes the total energy for $M_{1-u}Te_2$. The primary reason for this large, positive energy difference is the loss of inversion center in **6**, when compared to **3** and **4**. This feature allows complex orbital mixing among the Te_2 σ_p^* and all other occupied Te_2 orbitals and raises its energy in the conduction band. As more five-coordinate Te−Te groups are introduced, the bottom of the $M_{1-u}Te_2$ conduction band will rise and be replaced by the M e_g orbitals.

Disproportionation of $RhTe_2$

The phase diagram for the Rh−Te binary system shows that $RhTe_2$ undergoes disproportionation into a CdI_2-type $Rh_{1+x}Te_2$(h) and the pyrite-type $Rh_{1-u}Te_2$(c) at temperatures exceeding ca. 650 °C.[8] According to this study, both stoichiometric variables, x and u, increase with temperature up to 1075 °C, at which point the cubic phase decomposes peritectically. To analyze this process thermodynamically, we need to consider the relative free energies of the pyrite-type phase, $RhTe_2$(c), and some mixture of $Rh_{1+x}Te_2$(h) and $Rh_{1-u}Te_2$(c):

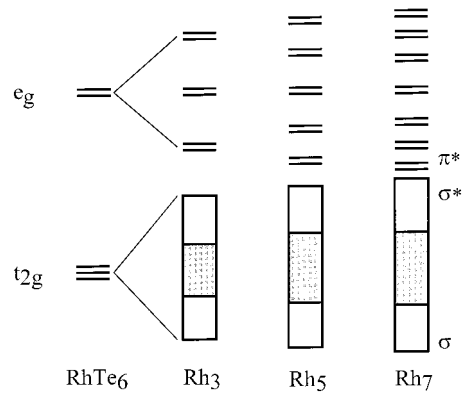

Figure 16. Qualitative orbital schemes to explain the curves in Figure 15 by examining the evolution of Rh t_{2g} and e_g orbitals as $[Rh_3Te_{12}]$, $[Rh_5Te_{18}]$, and $[Rh_7Te_{24}]$ oligomers are created. The t_{2g} orbitals broaden with Rh−Rh σ-bonding interactions at the bottom and σ-antibonding interactions at the top. The bottom of the e_g orbitals is Rh−Rh π antibonding.

$$RhTe_2(c) \xrightarrow{\Delta} aRh_{1+x}Te_2(h) + bRh_{1-u}Te_2(c)$$

This equation's stoichiometry demands that $a + b = 1$ and $ax = bu$. Although it is theoretically difficult to assess all thermodynamic variables needed for an evaluation of free energies, we can evaluate total valence electron energies of both sides of this equation. Figure 10a illustrates the trends in average electronic energy with x in $Rh_{1+x}Te_2$(h) and with u in $Rh_{1-u}Te_2$(c). For small values of x and u, the energy changes are nearly linear. $E(u)$ for $Rh_{1-u}Te_2$(c) rises as u increases because 6u Rh−(Te_2) interactions are lost; $E(x)$ for $Rh_{1+x}Te_2$(h) drops as x increases because 6x Rh−Te interactions are created. Combining the two curves in Figure 10a for various combinations of the stoichiometric coefficients a and b gives the curves in Figure 10b (a = 0.1, 0.25, and 0.4). As a increases (a corresponds to the fraction of the $Rh_{1+x}Te_2$(h) phase in the mixture), x decreases (i.e., fewer Rh atoms intercalate into the CdI_2-type arrangement) and the minimum value of ΔE for the disproportionation increases. From the results in Figure 10, we conclude that disproportionation of $RhTe_2$(c) is entropy driven (ΔE for the reaction above is always positive). Furthermore, more Rh atoms should transfer from $Rh_{1-u}Te_2$(c) to $Rh_{1+x}Te_2$(h) as temperature increases, which agrees with the observed phase diagram.[8] For the three data points highlighted in Figure 10b, which identify minima in the $\Delta E(x)$ curves for various values of a, the corresponding reactions are

$$RhTe_2(c) \rightarrow 0.10\ Rh_{1.40}Te_2(h) + 0.90\ Rh_{0.96}Te_2(c)$$
$$\Delta E_{min} = +0.059\ eV$$

$$RhTe_2(c) \rightarrow 0.25\ Rh_{1.20}Te_2(h) + 0.75\ Rh_{0.93}Te_2(c)$$
$$\Delta E_{min} = +0.163\ eV$$

$$RhTe_2(c) \rightarrow 0.40\ Rh_{1.11}Te_2(h) + 0.60\ Rh_{0.93}Te_2(c)$$
$$\Delta E_{min} = +0.269\ eV$$

These results demonstrate the strong relationship between metal oxidation states and orbital interaction energies. Although

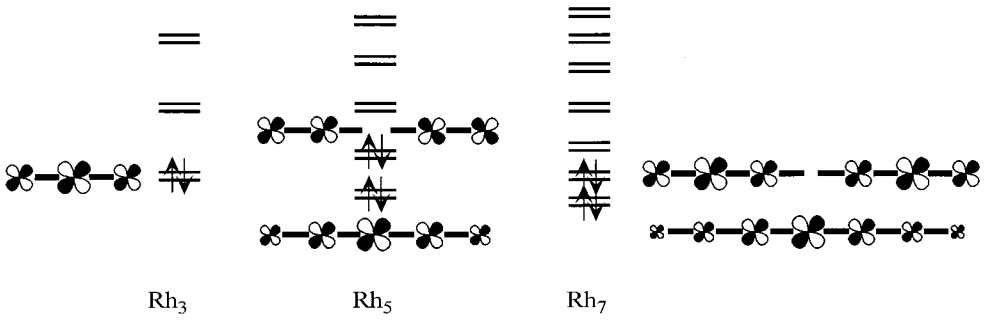

Figure 17. Valence e_g orbitals for the oligomers $[Rh_3Te_{12}]$, $[Rh_5Te_{18}]$, and $[Rh_7Te_{24}]$. Electrons show those orbitals that may be occupied for $Rh_{1+x}Te_2$.

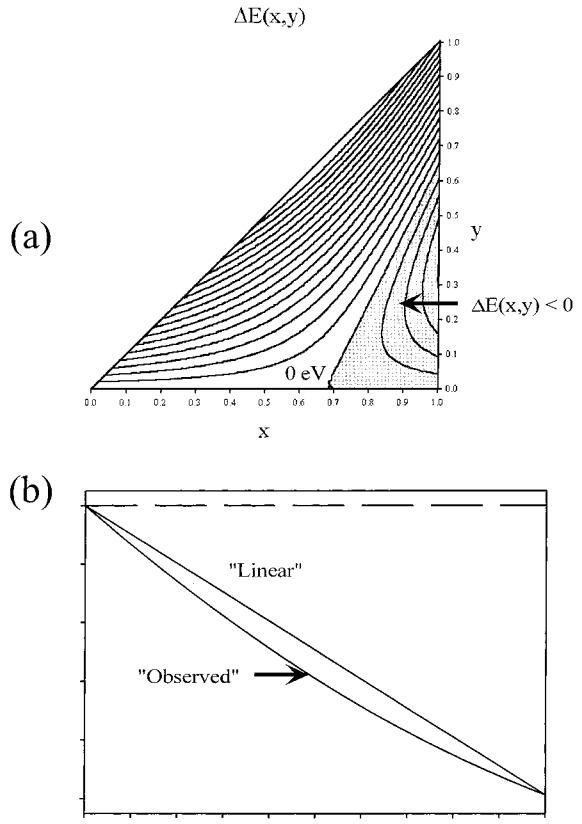

Figure 18. (a) Contour plot of the relative energies between $Rh_{1+x}Te_2$ and $Rh_{1+x-y}Te_2 + yRh$. The shaded region indicates negative values, i.e., regions in (x, y) space where $Rh_{1+x}Te_2$ is unstable with respect to disproportionation. (b) Total valence electron energy, $E(x)$, vs x for $Rh_{1+x}Te_2$. The observed curve is quadratic and is compared to a linear variation. The quadratic curve forms the basis for the contour plot in part a.

difficult to visualize on the energy scale of the plot in Figure 10a, neither curve is strictly linear over the entire range of u or x. As u increases in $Rh_{1-u}Te_2$(c), the oxidation state of Rh changes very little (see Table 4) but intermediate-range $Te_2\cdots Te_2$ interactions increase and cause an upward deviation of its energy curve. Also, as x increases in $Rh_{1+x}Te_2$(h), both Rh and Te are increasingly reduced. Since orbital interactions increase with $|\Delta E^{(0)}|^{-1}$ and since $E^{(0)}$(Rh 5d) rises with decreasing oxidation state, the strength of Rh−Te orbital interactions drops as x increases. Therefore, the energy curve for $Rh_{1+x}Te_2$(h) also deviates upward. We address this trend for $Rh_{1+x}Te_2$(h) in more detail in the next section. These two secondary effects, therefore, determine the shapes of the curves in Figure 10b.

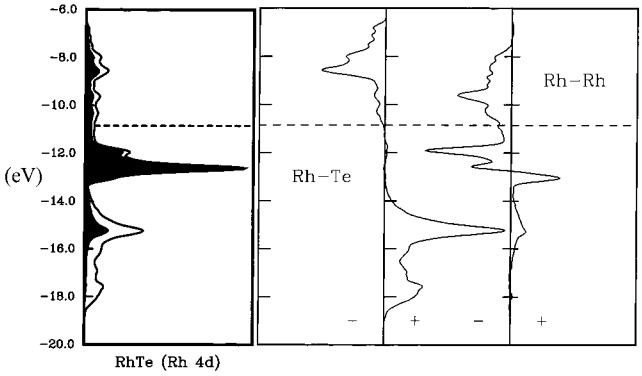

Figure 19. Total DOS curve and COOP curves for NiAs-type "RhTe". The dashed line indicates the calculated Fermi level. The projection of Rh 4d orbitals to the total DOS is also indicated. The COOP curves show overlap populations for the shortest Rh−Te and Rh−Rh contacts. (+) is a region of bonding interactions; (−) is a region of antibonding interactions.

Self-Intercalated $Rh_{1+x}Te_2$

Detailed crystallographic and thermodynamic studies of $Rh_{1+x}Te_2$ indicate continuous behavior for $0.15 \leq x \leq 0.84$.[7,10] Their structures are derived from the CdI_2-structure type with layers of octahedral holes occupied in an alternating pattern of 100% and 100x%. In fact, all structures can be indexed using a monoclinic unit cell that is a slight deviation from the orthorhombic cell of the 2D hexagonal lattice. This cell involves two MTe_2 layers in the hexagonal c direction with 2x additional M atoms between them. These additional metal atoms can occupy two crystallographically inequivalent sites in the space group $I2/m$ (Wyckoff sites 2a and 2d). For $x \leq 1/2$, the 2d site remains empty while the 2a site fills at the rate 2x. For $x > 1/2$, the 2d position fills at a rate 2x and the 2a site remains filled. Thus, crystallographic analysis indicates a nonrandom mechanism for filling the empty metal sites in the CdI_2-type structure.

In $Rh_{1+x}Te_2$, all Rh atoms are octahedrally coordinated by Te atoms. The observed filling pattern for $x \leq 1/2$ creates linear Rh_3 groups of three face-sharing octahedra. $Rh_{1.5}Te_2$, the upper limit for this field of structures, contains only these oligomers. For x exceeding $1/2$, longer oligomers are possible, e.g., Rh_7, Rh_{11}, ..., Rh_{4n+3}, etc., and approach quasi-infinite chains, as found in the NiAs structure type. Figure 11 illustrates the two different cases (black circles are 100% Rh; gray circles are partially occupied metal sites). We can formulate the compounds $Rh_{1+x}Te_2$ in two different ways to emphasize the presence of the trimers: (1) $x \leq 1/2$, $(Rh_3)_xRh_{1-2x}Te_2$; (2) $x \geq 1/2$, $(Rh_3)_{1-x}Rh_{4x-2}Te_2$. Table 5 summarizes the results of calculations on the entire series $Rh_{1+x}Te_2$. We have separated the Mulliken populations for Rh (symbolized by q) into three contributions: (1) the central Rh atom in each Rh_3 unit, $Rh^{(c)}$;

(2) the terminal Rh atoms in each trimer, $Rh^{(t)}$; and (3) the remaining Rh atoms, $Rh^{(o)}$. According to the site occupation pattern, the $Rh^{(c)}$ atoms represent the metal atoms between each "$RhTe_2$" layer, i.e., $Rh_{1+x}Te_2 = (Rh^{(c)})_x[(Rh^{(o)})_{1-2x}(Rh^{(t)})_{2x}Te_2]$. For $x < {}^1/_2$, these $Rh^{(c)}$ atoms are the most electron deficient among the Rh sites. The terminal positions of the trimers are the most electron rich. At $Rh_{1.5}Te_2$, no $Rh^{(o)}$ remain, and the distributions of electrons between $Rh^{(c)}$ and $Rh^{(t)}$ sites are nearly equal. For $x > {}^1/_2$, however, the opposite trend occurs. Electron density builds up on the $Rh^{(c)}$ sites rather than the $Rh^{(t)}$ sites.

Figure 12 illustrates the total DOS for $Rh_{1.5}Te_2$ and highlights the Rh z^2 projection and Te atomic orbital projections. The Fermi level lies just above the top of the z^2 band, which has Rh−Rh σ^* character and represents the top of the Rh t_{2g} orbitals. With the t_{2g} band formally filled, the distributions of electrons between $Rh^{(c)}$ and $Rh^{(t)}$ are essentially equal. For x values below ${}^1/_2$, electrons are removed from the top of the z^2 band, which, according to its orbital representation in the DOS, has its greatest component on $Rh^{(c)}$. Therefore, $Rh^{(t)}$ sites are more electron rich. On the other hand, for x values above ${}^1/_2$, electrons enter a Rh−Rh π^* band, which also has its greatest component on $Rh^{(c)}$. For these cases, $Rh^{(c)}$ is more electron rich.

The vacancy distribution also affects the local electronic structure at tellurium. Since the Te substructure changes very little, the average coordination of Te by Rh increases linearly with additional Rh atoms as $3 + 3x$. The coordination polyhedra, due to the pattern of site occupancies, will be one of the four environments, **7**−**10**, derived from a trigonal prism. For $x = 0$,

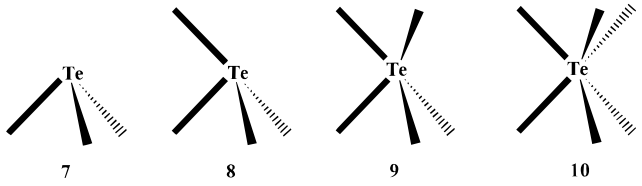

i.e., "$RhTe_2$", only **7** occurs. For $x < {}^1/_2$, the arrangement of Rh atoms allows **7**−**9** to coexist. $Rh_{1.5}Te_2$ (=Rh_3Te_4) represents a special case with 50% **8** and 50% **9**. For $x > {}^1/_2$, we find **8**−**10** as possible coordination environments for Te. Finally, at $x = 1$, i.e., "RhTe", only **10** is possible. As Table 5 shows, the Mulliken populations for the various Te atoms decrease by ca. 0.2 unit (electron) as the coordination number increases by 1. Furthermore, as x increases, the atomic population of Te increases monotonically for a given coordination environment.

An interesting result shown in Table 5 is the drop in the Fermi level from "$RhTe_2$" to $Rh_{1.08}Te_2$. Beyond $Rh_{1.08}Te_2$, E_F monotonically increases. We attribute the drop to the presence of four- and five-coordinate Te atoms, **8** and **9**, in the structures of $Rh_{1+x}Te_2$ for small x values. The addition of x Rh atoms to "$RhTe_2$" creates environments **8** and **9**, which removes $3x$ Te orbitals near the Fermi level ($3x$ levels become Rh−Te bonding; $3x$ levels become Rh−Te antibonding). Together with $3x$ Rh t_{2g} orbitals, there are now $6x$ new orbitals in the valence band which get only 9x electrons from the x Rh atoms. Thus, E_F drops for the initial stages of "self-intercalation" in "$RhTe_2$".

There are certainly other ways of filling the octahedral vacancies in the CdI_2 structure type in addition to the observed one. Such patterns have been identified in other chalcogenides, e.g., in titanium and chromium sulfides.[16] During the refinements of $Rh_{1+x}Te_2$, Abadie et al. considered two additional possibilities.[7] One alternative arrangement of filled and vacant metal sites, which maintains the CdI_2-type framework, leads to the space group $P\bar{3}m1$, and each vacant metal site fills at a rate x. The other alternative, with space group $P6_3/mmc$, considers a completely random distribution of vacancies throughout the metal substructure. These patterns are illustrated in Figure 13. The black circles represent completely occupied metal sites; the gray circles are partially occupied. Model A is the observed pattern and has two distinct representations for $x \leq {}^1/_2$ and $x \geq {}^1/_2$. Models B and C can be represented by a single pattern for the entire range of x.

The fraction of oligomers varies with x in $Rh_{1+x}Te_2$ for each of the three models mentioned above. Within the assigned unit cell, i.e., four layers of metal atoms, these fractions are illustrated in Figure 14A−C and the corresponding trends in total valence electron energy are shown in Figure 14D. Due to the distribution of vacancies in model A, for $x \leq {}^1/_2$, only Rh_3 units are possible. For $x > {}^1/_2$, the possible oligomers include Rh_{4n+3}, i.e., Rh_3, Rh_7, Rh_{11}, etc. The fraction of Rh_7 oligomers reaches as maximum at $x = 0.75$. In model B, the possible oligomers are Rh_{2n+3} and their fraction maximizes at $x = 0.50$. For model C, all oligomers are possible.

With respect to total valence electron energies, model A, in which the fraction of Rh_3 groups is maximized for all values of x, is slightly favored over model B for x less than ${}^1/_2$. As x grows above ${}^1/_2$, model A becomes even more favored because this pattern also minimizes the fraction of quasi-infinite chains in the structure. The totally random arrangement of occupied metal sites is significantly higher in energy and only becomes energetically competitive when x approaches 1.00, i.e., the NiAs type. As we have demonstrated, the difference between models A and B is the types of oligomers allowed by the distribution of vacancies. In Figure 15a, we illustrate the variation of total valence electron energies for $[Rh_3Te_{12}]$, $[Rh_5Te_{18}]$, and $[Rh_7Te_{24}]$ chains relative to a $[RhTe_6]$ octahedral fragment over all d electron concentrations. All curves are very similar. The trends from d^0 to d^6 per metal atom follow from the large σ overlap between adjacent z^2 orbitals: bonding at low d counts, antibonding at high d counts in the set of t_{2g} orbitals. As the length of the metal chain increases, the bandwidth of the z^2 orbitals increases. On the other hand, the trends from d^6 to d^{10} per metal atom follow from Rh−Te−Rh through-bond coupling. The bottom of the set of e_g orbitals has Rh−Rh π^* character and very little Rh−Te overlap. The top of this set is Rh−Rh π bonding but shows significant Rh−Te σ-antibonding character. Figure 16 shows the dispersion of Rh t_{2g} and e_g orbitals that leads to these relative energy curves.

A subtle difference between models A and B is that model B allows Rh_5 chains, while model A does not. Figure 15b illustrates the relative energies for $[Rh_3Te_{12}] + [Rh_7Te_{24}]$ and $2[Rh_5Te_{18}]$ chains. Between d^6 and d^7, the Rh_3 and Rh_7 chains are slightly preferred over the Rh_5 chains, which agrees with the structural models of Abadie for $Rh_{1+x}Te_2$.[7] We can understand this result by examining the qualitative orbital diagrams for the e_g bands of these three chains in Figure 17. The occupied orbitals are noted with electron symbols. The HOMO's for the Rh_3 and Rh_7 chains have similar features because the one node in the Rh_7 orbital creates two Rh_3 groups. The energy of the HOMO of the Rh_5 chain lies above those for Rh_3 and Rh_7 because its node creates two Rh_2 groups instead. Therefore, between d^6 and d^7 metal configurations, i.e., up to a ${}^1/_4$-filled e_g band, Rh_{4n+3} chains are preferred over Rh_{4n+1} chains.

(16) (a) Jellinek, F. *Acta Crystallogr.* **1957**, *10*, 620. (b) Flink, E.; Wiegers, G. A.; Jellinek, F. *Recl. Trav. Chim. Pays-Bas.* **1966**, *85*, 869. (c) Pearson, W. B. *The Crystal Chemistry and Physics of Metals and Alloys*; Wiley-Interscience: New York, 1972; p 461.

To study the energetics involved in setting the upper limit of composition, we have calculated the energy changes for the series of reactions

$$Rh_{1+x}Te_2 \rightarrow Rh_{1+x-y}Te_2 + yRh; \quad y \leq x$$

This disproportionation reduces the number of Rh−Rh antibonding interactions along the *c* axis as $Rh_{1+x-y}Te_2$ forms. Our results obtained the contour plot in Figure 18a, which shows $\Delta E(x,y)$ for this reaction. For the ranges, $0 \leq x \leq 1$ and $0 \leq y \leq x$, $\Delta E(x,y)$ varies between ca. −4 and +16 eV. The shaded region identifies negative $\Delta E(x,y)$ values and corresponds to the range of *x* and *y* where $Rh_{1+x}Te_2$ is unstable relative to $Rh_{1+x-y}Te_2$ and Rh. According to our results, this instability begins for *x* approximately 0.7, with small energy differences ($\Delta E(x,y) < 0.05$ eV) and becomes more significant as *x* increases. Although not in exact agreement with experiment (disproportionation must begin around $x = 0.84$), the phenomenon is clearly reproduced by our calculations.

To understand the upper limit in phase stability for $Rh_{1+x}Te_2$, we plot the trend in $E(Rh_{1+x}Te_2)$ vs *x* ($0 \leq x \leq 1$) in Figure 18b (note: this is an expanded version of Figure 10a). As Rh atoms are incorporated into the van der Waals gap of the CdI_2-type arrangement, the total valence electron energy drops due to more Rh−Te interactions, but the rate of decrease drops as *x* increases. This quadratic behavior in the total energy arises for two primary reasons: (1) As *x* increases, more repulsive (antibonding) orbital interactions between Rh atoms along the *c* axis occur and the Rh atoms become more reduced (see Table 5). (2) Rh−Te−Te−Rh through-bond coupling creates antibonding interactions between nearest neighbor Rh atoms, whose repulsive nature becomes more influential as the concentration of Rh increases. At the upper compositional limit, we reach the NiAs-type "RhTe". Figure 19 illustrates the total DOS and Rh−Te and Rh−Rh COOP curves for this hypothetical compound. The Rh e_g band contains one valence electron, which occupies Rh−Rh antibonding orbitals and essentially Rh−Te nonbonding orbitals. Furthermore, as Rh becomes more reduced, its atomic orbital energies increase relative to the atomic orbital energies of Te (see the H_{ii} values obtained from charge iteration calculations on "$RhTe_2$", $Rh_{1.5}Te_2$, and "RhTe" in Table 1). Since orbital interactions are measured as $S_{ij}^2/|\Delta E^{(0)}|$ and $\Delta E^{(0)}$ between Rh and Te atomic orbitals increases with *x*, the strength of Rh−Te orbital interactions are reduced as *x* increases and we observe the quadratic behavior of $E(x)$ in Figure 18b.

Conclusions

Semiempirical electronic structure calculations are able to elucidate the orbital interactions that influence the observed behavior of group 9 tellurides, M_xTe_2 ($0.75 \leq x \leq 2.00$). The distribution of vacancies in the various structures are closely linked to the structural moieties left behind, e.g., six- and four-coordinate Te−Te groups in $Rh_{1-u}Te_2$ and linear Rh_3 and Rh_7 groups in $Rh_{1+x}Te_2$. Analyses of the DOS curves, COOP curves, and band structures, coupled with a detailed examination of total valence electron energy surfaces, provide the rationale for their behavior. We are continuing to generalize this procedure to other intermetallic systems by considering vacancies in extended solids from a local chemical perspective.

Acknowledgment. This work was supported by the National Science Foundation under Grant DMR-96-27161.

IC990652S